Experimental Validation of Single Base Station 5G mm Wave Positioning: Initial Findings

Downloaded from: https://research.chalmers.se, 2026-04-06 17:40 UTC

Citation for the original published paper (version of record):

Ge, Y., Chen, H., Jiang, F. et al (2022). Experimental Validation of Single Base Station 5G mm Wave Positioning: Initial Findings. 2022 25th International Conference on Information Fusion, FUSION 2022. http://dx.doi.org/10.23919/FUSION49751.2022.9841230

N.B. When citing this work, cite the original published paper.

research.chalmers.se offers the possibility of retrieving research publications produced at Chalmers University of Technology. It covers all kind of research output: articles, dissertations, conference papers, reports etc. since 2004. research.chalmers.se is administrated and maintained by Chalmers Library

(article starts on next page)

Experimental Validation of Single Base Station 5G mmWave Positioning: Initial Findings

Yu Ge*, Hui Chen*, Fan Jiang*, Meifang Zhu†, Hedieh Khosravi†, Simon Lindberg‡,
Hans Herbertsson§, Olof Eriksson§, Oliver Brunnegård§, Bengt-Erik Olsson¶, Peter Hammarberg¶,
Fredrik Tufvesson†, Lennart Svensson*, Henk Wymeersch*
*Department of Electrical Engineering, Chalmers University of Technology, Gothenburg, Sweden,
†Department of Electrical and Information Technology, Lund University, Lund, Sweden,
‡Qamcom, Gothenburg, Sweden, §Veoneer, Gothenburg, Sweden, ¶Ericsson Research, Gothenburg, Sweden

***Abstract*—5G cellular networks can utilize millimeter wave signals, and support large bandwidths and large antenna arrays, which provide more geometric-based signals and higher delay and angle resolutions. These merits bring new opportunities in positioning the user with limited infrastructure through the use of combined angle and delay information. However, there are many practical challenges to overcome, in order to have a functioning single base station 5G mmWave positioning system. In this paper, we describe a deployed single base station mmWave positioning system, and provide an example of the measurement data. Furthermore, we perform measurement validation on a limited measurement data set by performing base station localization. Additional evaluations performed on simulation model data provide guidelines on the required size of the data set and receiver antenna configuration, which will be implemented in upcoming measurements.**

***Index Terms*—5G mmWave positioning system, experiments, base station localization, preliminary findings.**

I. Introduction

Absolute and relative positioning of vehicles is required to support a variety of autonomous drive (AD) and advanced driver assistance system (ADAS) services. While accurate relative positioning is enabled with sensors such as radar, camera, lidar [1], and inertial measurement unit (IMU), absolute positioning relies on an external reference. Such a reference can be in the form of a global map (so that local features can be associated in the global map), or in the form of satellites in a global navigation satellite system (GNSS) [2]. When maps are erroneous or out-of-date [3] or insufficiently many satellites are in view, global positioning is compromised [4], leading to safety risks or driver comfort degradation. Hence, alternative absolute positioning sensors, complementing high-resolution maps and GNSS are of high importance.

Cellular communication infrastructure can serve as such a complementary sensor, provided sufficient accuracy, latency and reliability [5], [6]. Since 3GPP Release 16, the availability of large bandwidths (up to 400 MHz) at mmWave frequencies (e.g. around 28 GHz) in 5G, combined with new dedicated positioning reference signals (PRSs) and procedures, enables unparalleled positioning accuracy [7]. Positioning can be based on the combination of delay (e.g., time-difference-of-arrival (TDOA) or round-trip-time (RTT)) and angular (e.g., angles-of-arrival (AOA) or angles-of-departure (AOD)) measurements. TDOA-based positioning with several base stations (BSs) provides accuracies down to 1.5 m (90% performance) in urban scenarios, based on signals with only 100 us duration [8]. Further improvements can be provided by denser BS deployments [9] or by harnessing angle information [8]. Studies reporting experimental validation of 5G mmWave positioning have been limited [10], [11], and most existing works rely on simulations [8], [12].

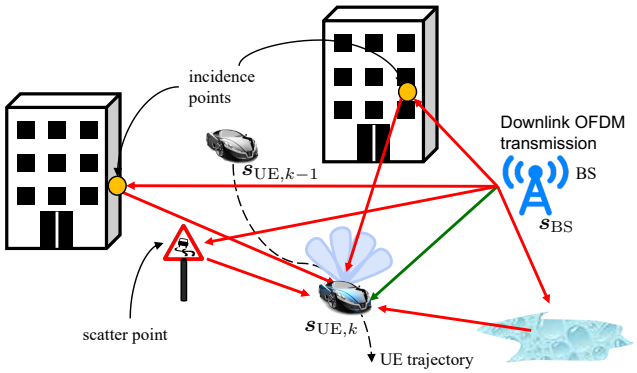

Fig. 1. A single BS 5G mmWave downlink scenario with a few landmarks, where signals sent from BS can reach the UE via the LOS (the green line) and NLOS (red lines) paths.

In contrast to communication, where a link can be provided with a single BS, positioning generally requires several BSs. For example, 3D TDOA-based positioning requires at least 4 visible BSs in order to solve for the user equipment (UE) 3D position and 1D clock bias. To reduce the reliance on infrastructure, signals and methods for positioning with fewer BSs have been intensely investigated in recent years [13]. A fundamental result is that positioning with a single BS is possible, provided (i) both the BS and UE are equipped with 2D arrays; (ii) there are at least one resolvable multi-path component in the environment [14], since fundamentally each non-line-of-sight (NLOS) path provides rank-1 position information, irrespective if the signal source is known or not [15].

In this paper, we report initial results towards the validation of single-BS vehicular positioning with downlink 5G mmWave signals, as part of an industry-academia collaboration project. Our validation comprised a UE mounted on a driving vehicle,

receiving downlink signals from a deployed 5G mmWave BS. While our study is limited to off-line processing, we identify several important gaps between the theoretical assumptions and the real-world behavior of positioning systems. The purpose of this paper is to report our preliminary findings, which in turn raises a number of interesting research questions and refined models for theoretical work.

Notations: Scalars (e.g., x) are denoted in italic, vectors (e.g., $\boldsymbol{x}$) are denoted in bold lower-case letters, and matrices (e.g., $\boldsymbol{X}$) are denoted in bold capital letters. The conjugate transpose is denoted by $(\cdot)^{\mathsf{T}}$, the Euclidean norm is denoted by $\|\cdot\|$, the n-th component of a vector is denoted by $[\cdot]_n$, a Gaussian density with mean $\boldsymbol{u}$ and covariance $\boldsymbol{\Sigma}$, evaluated in value $\boldsymbol{x}$, is denoted by $\mathcal{N}(\boldsymbol{x}; \boldsymbol{u}, \boldsymbol{\Sigma})$.

II. System models

We consider a 5G mmWave downlink scenario, with a single fixed BS and a single moving UE, as shown in Fig. 1. Both of them are equipped with an uniform rectangular array (URA). The considered systems models are introduced in this section.

A. BS and UE Models

With respect to a fixed global reference coordinate system, the transmitter URA at the BS side is centered at the 3D position $\boldsymbol{p}_{\text{BS}} = [x_{\text{BS}}, y_{\text{BS}}, z_{\text{BS}}]^{\mathsf{T}}$, and has Euler angles $(\alpha_{\text{BS}}, \beta_{\text{BS}}, \gamma_{\text{BS}})$ with the order of roll, pitch and yaw, representing the direction of the URA [16]. Therefore, the state of the BS can be described as $\boldsymbol{s}_{\text{BS}} = [\boldsymbol{p}_{\text{BS}}^{\mathsf{T}}, \alpha_{\text{BS}}, \beta_{\text{BS}}, \gamma_{\text{BS}}]^{\mathsf{T}}$. Similarly, the state of the UE at time step k (with period Δ_t) can be modeled as $\boldsymbol{s}_{\text{UE},k} = [\boldsymbol{p}_{\text{UE},k}^{\mathsf{T}}, \alpha_{\text{UE},k}, \beta_{\text{UE},k}, \gamma_{\text{UE},k}, b_k]^{\mathsf{T}}$, with $\boldsymbol{p}_{\text{UE},k} = [x_{\text{UE},k}, y_{\text{UE},k}, z_{\text{UE},k}]^{\mathsf{T}}$ and $(\alpha_{\text{UE},k}, \beta_{\text{UE},k}, \gamma_{\text{UE},k})$ denoting the position of the center of the receiver URA at the UE side and its orientation, respectively, and b_k denoting the clock bias.

B. Signal Models

At time step k, the BS sends downlink signals to the UE, and these signals can reach the UE directly, and/or reflected or scattered by landmarks in the environment, which are the LOS path and NLOS paths, respectively. When OFDM transmissions are considered, received signal at subcarrier κ for the g-th OFDM symbol at time step k can be expressed as [17]

$$y_{\kappa,g,k} = \boldsymbol{w}_{\text{UE},g,k}^{\mathsf{T}} \boldsymbol{H}_{\kappa,k} \boldsymbol{w}_{\text{BS},g,k} s_{\kappa,g} + n_{\kappa,g,k} \tag{1}$$

where $\boldsymbol{w}_{\text{UE},g,k}$ is the UE combiner, $\boldsymbol{w}_{\text{BS},g,k}$ the BS precoder, $s_{\kappa,g}$ the pilot signal, $n_{\kappa,g,k}$ is white Gaussian noise, and $\boldsymbol{H}_{\kappa,k}$ the channel matrix

$$\boldsymbol{H}_{\kappa,k} = \sum_{i=0}^{I_k-1} \rho_k^i \boldsymbol{a}_{\text{R}}(\boldsymbol{\theta}_k^i) \boldsymbol{a}_{\text{T}}^{\mathsf{T}}(\boldsymbol{\phi}_k^i) e^{-\jmath 2\pi\kappa\Delta_f \tau_k^i} \tag{2}$$

where $\boldsymbol{a}_{\text{R}}(\cdot)$ and $\boldsymbol{a}_{\text{T}}(\cdot)$ are the steering vectors of the receiver and transmitter URAs, respectively, and Δ_f is the subcarrier spacing. Moreover, there are I_k paths in total. The LOS path corresponds to $i = 0$, and the NLOS paths to $i > 0$. Each path i can be described by a complex gain ρ_k^i, a time-of-arrival (TOA) τ_k^i, an AOA pair $\boldsymbol{\theta}_k^i = [\theta_{\text{az},k}^i, \theta_{\text{el},k}^i]^{\mathsf{T}}$ in azimuth and elevation, and an AOD pair $\boldsymbol{\phi}_k^i = [\phi_{\text{az},k}^i, \phi_{\text{el},k}^i]^{\mathsf{T}}$ in azimuth and elevation.

C. Geometric Models

The TOAs, AOAs, AODs depend on the geometric relationships among the BS, the UE and the surrounding environment. Specifically, TOA τ_k^i can be defined as

$$\tau_k^i = \begin{cases} \|\boldsymbol{p}_{\text{BS}} - \boldsymbol{p}_{\text{UE},k}\|/c + b_k & i = 0 \\ \|\boldsymbol{p}_{\text{inc},k}^i - \boldsymbol{p}_{\text{UE},k}\|/c + \|\boldsymbol{p}_{\text{inc},k}^i - \boldsymbol{p}_{\text{BS}}\|/c + b_k & i \neq 0 \end{cases}, \tag{3}$$

where $\boldsymbol{p}_{\text{inc},k}^i$ is the position of the incidence point of the i-th path on the corresponding landmark at time step k, and c is the speed of light. As $\boldsymbol{\theta}_k^i$ is determined by the arrival direction in the local coordination system of the UE, the arrival direction can be calculated by

$$\boldsymbol{q}_{\text{AOA},k}^i = \begin{cases} \boldsymbol{R}_{\text{UE},k}(\boldsymbol{p}_{\text{BS}} - \boldsymbol{p}_{\text{UE},k}) & i = 0 \\ \boldsymbol{R}_{\text{UE},k}(\boldsymbol{p}_{\text{inc},k}^i - \boldsymbol{p}_{\text{UE},k}) & i \neq 0 \end{cases}, \tag{4}$$

where $\boldsymbol{R}_{\text{UE},k}$ is the rotation matrix from the global reference coordinate system to the local coordination system of the UE at time step k, which can be determined by $(\alpha_{\text{UE},k}, \beta_{\text{UE},k}, \gamma_{\text{UE},k})$ as [16]

$$\boldsymbol{R}_{\text{UE},k} = \begin{bmatrix} \cos\gamma_{\text{UE},k} & -\sin\gamma_{\text{UE},k} & 0 \\ \sin\gamma_{\text{UE},k} & \cos\gamma_{\text{UE},k} & 0 \\ 0 & 0 & 1 \end{bmatrix} \times \tag{5}$$
$$\begin{bmatrix} \cos\beta_{\text{UE},k} & 0 & \sin\beta_{\text{UE},k} \\ 0 & 1 & 0 \\ -\sin\beta_{\text{UE},k} & 0 & \cos\beta_{\text{UE},k} \end{bmatrix} \begin{bmatrix} 1 & 0 & 0 \\ 0 & \cos\alpha_{\text{UE},k} & -\sin\alpha_{\text{UE},k} \\ 0 & \sin\alpha_{\text{UE},k} & \cos\alpha_{\text{UE},k} \end{bmatrix}.$$

Then, $\boldsymbol{\theta}_k^i$ can be defined as

$$\theta_{\text{az},k}^i = \arctan2([\boldsymbol{q}_{\text{AOA},k}^i]_2, [\boldsymbol{q}_{\text{AOA},k}^i]_1), \tag{6}$$
$$\theta_{\text{el},k}^i = \arcsin([\boldsymbol{q}_{\text{AOA},k}^i]_3, \|\boldsymbol{q}_{\text{AOA},k}^i\|). \tag{7}$$

Similarly, the departure direction can be calculated by

$$\boldsymbol{q}_{\text{AOD},k}^i = \begin{cases} \boldsymbol{R}_{\text{BS}}(\boldsymbol{p}_{\text{UE},k} - \boldsymbol{p}_{\text{BS}}) & i = 0 \\ \boldsymbol{R}_{\text{BS}}(\boldsymbol{p}_{\text{inc},k}^i - \boldsymbol{p}_{\text{BS}}) & i \neq 0 \end{cases}, \tag{8}$$

where $\boldsymbol{R}_{\text{BS}}$ is the rotation matrix from the global reference coordinate system to the local coordination system of the BS, defined in similar fashion as (5). and $\boldsymbol{\phi}_k^i$ can be defined as

$$\phi_{\text{az},k}^i = \arctan2([\boldsymbol{q}_{\text{AOD},k}^i]_2, [\boldsymbol{q}_{\text{AOD},k}^i]_1), \tag{9}$$
$$\phi_{\text{el},k}^i = \arcsin([\boldsymbol{q}_{\text{AOD},k}^i]_3, \|\boldsymbol{q}_{\text{AOD},k}^i\|). \tag{10}$$

III. System Components

The designed 5G mmWave positioning system consists of a transmitter antenna array system at the BS side, a receiver antenna array system, and a GNSS system at the UE side. The BS sends signals to the UE, and the GNSS system provides the ground truth of the UE state every time step. In this section, details about the system components are described.

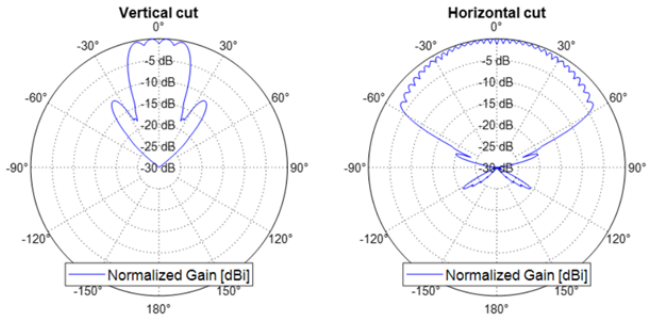

Fig. 2. Horizontal and vertical cuts of the BS beam pattern envelope.

A. Transmitter Antenna Array System at the BS

The BS has a commercial tower-mounted integrated Active Antenna System (AAS) radio unit (Ericsson AIR 5322), connected to a remote baseband unit that controls the signal generation, scheduling, etc.

1) Beam Description: The AAS is configured to use a phased array antenna module with 16×24 dual-polarized antenna elements. Analog beamforming is implemented, and the AAS can produce 4×34 (elevation×azimuth) beams. The 3 dB beamwidth of the center beam is $4.1°$ in azimuth and 10.4 degrees in elevation, and the aggregated beamwidth is approximately $\pm$ $60°$ in azimuth and $\pm$ $15°$ in elevation, as illustrated in Fig. 2.

2) Signal Description: In the custom-built non-commercial demo beam-controlling software, all 136 traffic beams are swept with 40 ms periodicity and configurable repetition of each beam. At the beginning of each beam sweep, Synchronization Signal/Physical Broadcast Channel block (SSB) [18] is transmitted on dedicated beams with 40 ms periodicity. The SSB contains synchronization signals and system information, which enable the UE to acquire time and frequency synchronization and perform random access procedure for network connection. To allow for channel estimation for each transmit beam, channel state information reference signal (CSI-RS) is transmitted at the UE. The CSI-RS is implemented according to the 3GPP NR 5G standard [18], configured to produce a pseudorandom sequence and mapped to QPSK symbols transmitted on every fourth subcarrier. The CSI-RS is transmitted on each of the four phase-locked component carriers, producing a total bandwidth of 4×100 MHz. With 120 kHz subcarrier spacing and the standardized guard band between carriers, a total of 4×198 subcarriers are used for channel state acquisition.

3) Uncertainties and Impact for Positioning: There are a number of uncertainties that have an impact on the accuracy of the channel parameter estimation. They relate both to the AAS and its deployment. From the AAS perspective, each device experiences small individual variations naturally occurring in the production and calibration process. These variations have an impact on the properties of the beam shape produced by the AAS. From the wireless communication perspective, these variations have an insignificant impact on the system performance and regulatory requirements. However, it may not be the case for high accuracy positioning exploiting angular information of the incoming radio wave, which is derived using beam directions and underlying beam shape. In particular, for communication $\boldsymbol{a}_{\mathrm{T}}^{\mathsf{T}}(\boldsymbol{\phi}_k^i)\boldsymbol{w}_{\mathrm{BS},g,k}$ is only known approximately (see Fig. 2), while neither $\boldsymbol{a}_{\mathrm{T}}(\boldsymbol{\phi}_k^i)$ or $\boldsymbol{w}_{\mathrm{BS},g,k}$ are characterized precisely, precluding the use of super-resolution methods. Hence, any characterization of the deployed AAS and the produced beams have not been performed, instead, we rely on the beam properties designed and obtained through simulations.

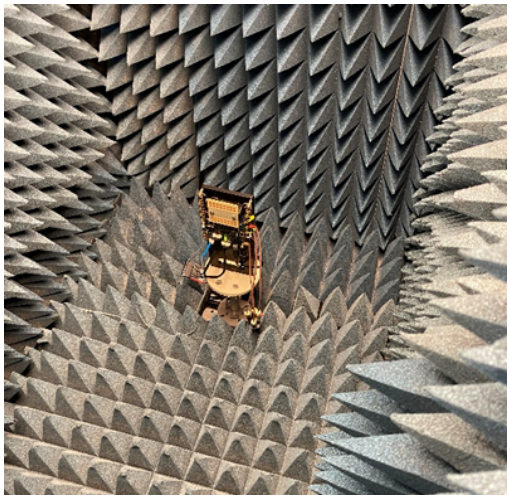

Fig. 3. The UE antenna array was put in a chamber with absorbers to measure the antenna response.

From the deployment perspective, not knowing the exact position of the BS can induce large positioning errors. When exploiting angular information for positioning, both the coordinate and the orientation of the AAS need to be known. For cell planning, communication, or coarse positioning, the requirement of the accuracy of the information on the above entities is not large. However, if high accuracy positioning is targeted, extra care needs to be taken when deploying nodes, and dedicated surveying is required to reduce uncertainties. This will inevitably increase the cost of deploying the network. For measurements performed and presented in this paper, we reuse a deployment intended for communication, where highly accurate surveying of the location and orientation of the AAS has not been performed.

B. Receiver Antenna Array System at the UE

The UE comprises a Sivers IMA 5G mmWave system test platform (STP02800 R1.0), modified to acquire signals from real 5G mmWave BSs.

1) Beam Description: The UE is equipped with two 2×8 URAs, where only one of them is active and the other serves as a backup. We have characterized the beam pattern in the azimuth domain by measuring the antenna response in a chamber with absorbs, where a positioner is utilized to ensure the antenna scan per degree in the azimuth domain, as shown in Fig. 3. The center frequency is 27.2 GHz, and the bandwidth

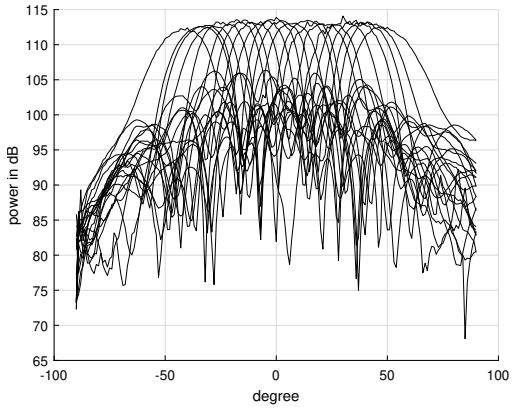

Fig. 4. Visualization of the UE beam pattern. Antenna response of the 21 beams at 27.2 GHz.

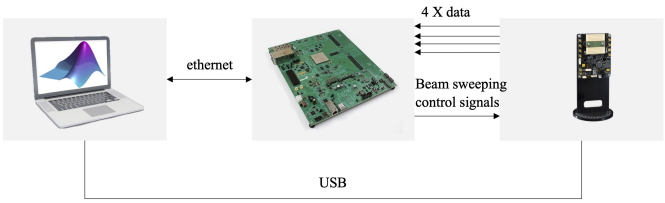

Fig. 5. Setup for signal acquisition. The RFSoC stores the sampled data from the UE, and controls the beam sweeping sequence. The PC downloads samples from the RFSoC to its hard drive.

is 400 MHz, which is divided into 3168 sub-bands. Antenna weighting vectors are applied to the 16 antenna elements to generate 21 different beams, which cover the range from $-45°$ to $45°$. The characterized beam pattern is shown in Fig. 4. It can be noted that a slightly wider beamwidth for each beam is obtained from measurements, and the beams are not distributed over $90°$ with a constant step size. For example, the two nearby beams can sometimes be similar, so we might not necessarily sweep all the beams during the measurements.

2) Signal Processing Description: The transmitted signal from the BS with 40 ms periodicity consists of an initial synchronization part, followed by the part performing BS beam sweep with CSI-RS transmissions. The synchronization part, carrying SSB, has a duration of 2.125 ms, immediately followed by the 37.875 ms of CSI-RS transmission. The signal acquisition at the UE side is controlled via a computer and a radio frequency system-on-chip (RFSoC), which also controls the beam sweeping sequence, as illustrated in Fig. 5. The UE samples data during 40 ms and stores the samples on the RFSoC, from where the PC downloads them to its hard drive.

Then the synchronization process starts. The synchronization of the UE with the BS is done in several steps. Firstly, the carrier frequency difference is estimated, and a first timing synchronization is done, finding out which sample is the first for each symbol. Then, the symbol numbers are calculated to find the beginning of the frame. Finally, the difference in sampling rate between the BS and the UE is calculated and adjusted. All the steps are done using the Primary Synchronization Signal (PSS) part of the SSB, except the symbol numbers which can be found using the Secondary Synchronization Signal (SSS) and Physical Broadcast Channel (PBCH). Once the synchronization has been completed, the RFSoC keeps track of the samples and makes sure that the start of the sampling period is aligned with the start of the signal from the BS. This synchronization is also important to match the beam sweeping of the UE and BS, and to assure that the beam switching is done during the cyclic prefix of a symbol. For positioning, the CSI-RS data is extracted and demodulated. This data is then used for channel estimation for each beam pair, which in turn is used in the positioning algorithms.

TABLE I
AVERAGE MEASUREMENT UNCERTAINTIES REPORTED BY OXTS DURING THE TEST

Heading (yaw) accuracy (deg)	1.136
Pitch accuracy (deg)	0.052
Roll accuracy (deg)	0.060
Position accuracy north (m)	0.194
Position accuracy east (m)	0.187
Position accuracy down (m)	0.245

3) Uncertainties and Impact for Positioning: In contrast to the BS, the complex element response and beam response at the UE is fully characterized. Hence, both $\boldsymbol{w}_{\mathrm{UE},g,k}$ and $\boldsymbol{a}_{\mathrm{R}}(\boldsymbol{\theta}_k^i)$ are known, opening up possibilities for super-resolution processing [19]–[21]. While collecting the measurements, the main challenge is to maintain the synchronization between the BS and UE. This is challenging due to the relative drift of the sampling clocks. Even though most of the effect is handled during the synchronization steps, there is still a small residual drift remaining. This drift can cause the sampling to shift hundreds of samples in just a few minutes, which can have a large impact on the positioning calculations.

C. Ground Truth Collection

The UE used in the test was equipped with the OXTS 3003G V2.0 [22] GNSS system to capture an accurate ground truth, providing accuracy down to 0.1 m. The OXTS system combines a GNSS receiver, an IMU and real-time-processing on-board processing. The system utilizes a Kalman filter to combining the IMU and GNSS inputs, providing a real-time estimate of the position in between GNSS position updates. Real-time kinematic (RTK) corrections are provided via the SWEPOS network-RTK service [23] to enhance the position accuracy. The average measurement uncertainties reported by the OXTS during the test are summarized in Table I.

IV. METHODOLOGY

While our purpose is to position the UE, from Section III, it is apparent that the BS location and orientation is more uncertain (on the order of around 1-2 meters and a few degrees, respectively) than the UE location and orientation uncertainty (see Table I). Hence, to understand the quality of the measurements, we use the received signals at the UE to determine the position of the BS and then compare with the a priori BS position information.

A. Channel Estimation

To perform the channel estimation from (1), beam sweeping schemes over each subcarrier are designed. Specifically, the BS and the UE use codebooks $\mathcal{C}_{\text{BS}} = \{\boldsymbol{\varphi}_1, \ldots, \boldsymbol{\varphi}_{|\mathcal{C}_{\text{BS}}|}\}$ ($\boldsymbol{\varphi}_m = [\varphi_{\text{az},m}, \varphi_{\text{el},m}]^{\mathsf{T}}$) with the size of $|\mathcal{C}_{\text{BS}}|$ and $\mathcal{C}_{\text{UE}} = \{\vartheta_1, \ldots, \vartheta_{|\mathcal{C}_{\text{UE}}|}\}$ ($\boldsymbol{\vartheta}_m = \vartheta_{\text{az}}$ due to a low elevation angle resolution) with the size of $|\mathcal{C}_{\text{UE}}|$, respectively. For each beam sent at the BS, $|\mathcal{C}_{\text{UE}}|$ OFDM symbols are sent to make sure the beam sweeping is completed at the UE side, resulting in $G = |\mathcal{C}_{\text{BS}}| \times |\mathcal{C}_{\text{UE}}|$ transmitted OFDM symbols for each measurement.

During the transmission of the g-th ($g = 1, 2, \cdots, G$) OFDM symbol at time k, the g-th pair of beam sweeping is accomplished. We denote $\boldsymbol{w}_{\text{BS},g}$ to the transmit beam towards a local 2D angle $\boldsymbol{\varphi}_m$, and $\boldsymbol{w}_{\text{UE},g}$ to the receive beam from the local azimuth angle $\vartheta_{\text{az},m}$. Note that the BS is repeating the sweeping process, while UE only collectes G OFDM symbols after synchronization. With the pilot $s_{\kappa,g}$, the beamspace channel over the κ-th subcarrier, i.e., $h_{\kappa,g,k} = \boldsymbol{w}_{\text{UE},g,k}^{\mathsf{T}} \boldsymbol{H}_{\kappa,k} \boldsymbol{w}_{\text{BS},g,k}$ is given by

$$\hat{h}_{\kappa,g,k} = \frac{s_{\kappa,g}^* y_{\kappa,g,k}}{|s_{\kappa,g}|^2} = h_{\kappa,g,k} + \frac{s_{\kappa,g}^* n_{\kappa,g,k}}{|s_{\kappa,g}|^2}. \tag{11}$$

Without complete knowledge of the transmit and receive beams, we rely on the resolution of the used beams to estimate the angles and delays. Specifically, when the g-th beam pair matches the physical propagation path at time k, the received power over all subcarriers will be strong. Therefore, with the estimated beamspace channel in (11), the strongest propagation path at time k, i.e.,

$$\hat{i}_k = \arg\max_g \sum_\kappa |\hat{h}_{\kappa,g,k}|^2, \tag{12}$$

will have the associated AOD $\hat{\boldsymbol{\phi}}_k^i = \boldsymbol{\varphi}_p$ and AOA $\hat{\theta}_k^i = \vartheta_q$ where $p = \lfloor (\hat{i}_k - 1)/|\mathcal{C}_{\text{UE}}| + 1 \rfloor$ and $q = \hat{i}_k - (p-1)|\mathcal{C}_{\text{UE}}|$. In addition, for each beam-pair received signal, the phase changes linearly with the subcarrier index as indicated in (2), where the slope is scaled by $2\pi\Delta_f \tau_k^i$. Therefore, the propagation delay corresponds to the physical path can be obtained through the linear regression approaches. More specifically, for the strongest beam pair $\hat{i}_k$, we obtain $[\hat{a}, \hat{b}] = \arg\min_{(a,b)} \sum_\kappa \| \angle \hat{h}_{\kappa,\hat{i}_k,k} - a\kappa - b \|^2$. The associated delay will be $\hat{\tau}_k^i = -a/(2\pi\Delta_f)$. The AOAs/AODs and delays of other MPCs can be obtained in the similar way.

B. BS Localization

When the UE arrivals at a new location $\boldsymbol{p}_{\text{UE},l}$, the OXTS system provides the measurement of $\boldsymbol{s}_{\text{UE},l}$. The UE receives the signals sent from the BS and does the channel estimation, providing measurements $\mathcal{Z}_l$. Although all elements in $\mathcal{Z}_l$ contain information on $\boldsymbol{s}_{\text{BS}}$, incidence points for NLOS paths are unavailable, and there are no reference reflectors or points in the environment. Therefore, all NLOS paths cannot be used, and we can only use the LOS path

$$\boldsymbol{z}_l^0 = [\hat{\tau}_l^0, (\hat{\boldsymbol{\theta}}_l^0)^{\mathsf{T}}, (\hat{\boldsymbol{\phi}}_l^0)^{\mathsf{T}}]^{\mathsf{T}}. \tag{13}$$

When considering L different UE locations, $\boldsymbol{s}_{\text{BS}}$ can be estimated by applying a maximum a posteriori (MAP) estimator

$$\begin{aligned}
\hat{\boldsymbol{s}}_{\text{BS}} &= \arg\max_{\boldsymbol{s}_{\text{BS}}} p(\boldsymbol{s}_{\text{BS}} | \boldsymbol{s}_{\text{UE},1:L}, \boldsymbol{z}_{1:L}^0) \\
&= \arg\max_{\boldsymbol{s}_{\text{BS}}} p(\boldsymbol{s}_{\text{BS}}) p(\boldsymbol{s}_{\text{UE},1:L}) p(\boldsymbol{z}_{1:L}^0 | \boldsymbol{s}_{\text{UE},1:L}, \boldsymbol{s}_{\text{BS}}) \\
&= \arg\max_{\boldsymbol{s}_{\text{BS}}} p(\boldsymbol{s}_{\text{BS}}) \prod_{l=1}^{L} p(\boldsymbol{s}_{\text{UE},l}) p(\boldsymbol{z}_l^0 | \boldsymbol{s}_{\text{UE},l}, \boldsymbol{s}_{\text{BS}}),
\end{aligned} \tag{14}$$

where $p(\boldsymbol{s}_{\text{BS}})$ denotes the (uniform) prior of $\boldsymbol{s}_{\text{BS}}$, and $p(\boldsymbol{s}_{\text{UE},l})$ denotes the density of the $\boldsymbol{s}_{\text{UE},l}$, with the mean measured by the OXTS system, the covariance of the coordinates and directions is provided as the in Table I, and the covariance of the clock bias is determined by the synchronization process.

V. Results

In this section, the real test environment is described, channel estimation results, and BS localization results of both simulated measurements and the channel estimations of the collected measurements are shown.

A. Test Environment

The tests were carried out at Ideon scientific park, Lund, as shown in Fig. 6, where the BS was fixed at coordinate (55°42'58.6"N 13°13'32.9"E) on a signal tower with a height of 30 m. The antenna array at the BS was facing north with a $12°$ tilt angle. The UE can move within an area for static and dynamic measurements, where the center was around 140 m away from the BS coordinate. It was an effective measurement area for positioning purposes due to the large storey buildings that can give significant reflections. At the same time, for some directions, the LOS was guaranteed. We placed the UE at two different locations, and collected 10 groups of received signals at each location.

The UE antenna array was installed on to the roof of the test host vehicle with the antenna array front looking. An absorption shield was provided to avoid multipath from BS signals in the host hood. The array angle was aligned with the direction of the vehicle and corresponding GPS yaw, pitch, and roll. The relative position of the UE antenna with respect to the host vehicle's GPS point on the rear axis, in longitudinal, lateral, and height position was geometrically measured. The installation provided some minor errors, for instance, the relative position of the UE antenna with respect to the GPS point, and the antenna direction accuracy with respect to the direction of the host vehicle and the heading given by the GPS. However, those possible errors are minor and fixed for all measurements, thus can be ignored.

B. Simulation Environment

To validate and understand the measurement results, we performed a theoretical analysis of the BS localization based on simulated data, and compare it with the BS localization results of the measurement data. We directly generate the channel parameters according to the experimental setup. We consider a simulated scenario with a single BS located at

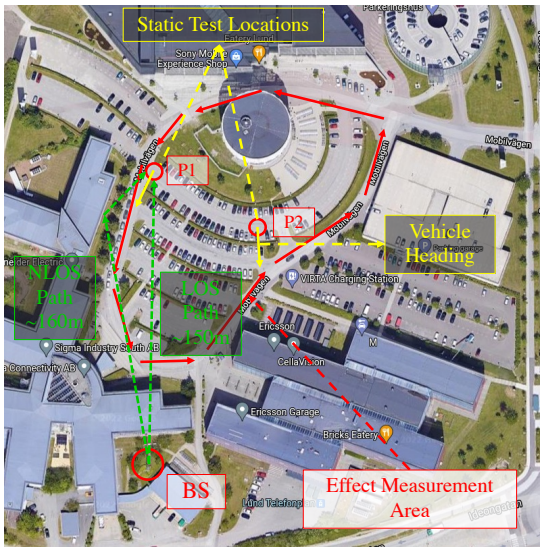

Fig. 6. The test environment at Ideon scientific park, Lund. The BS is visible in the bottom left part of the figure. Two example locations of the UE are shown as P1 and P2, with the vehicle heading (yaw) indicated with a yellow arrow. For P1, the LOS path as well as a suspected specular reflection are shown in green.

$\boldsymbol{p}_{\text{BS}} = [140\text{ m}, 0, 30\text{ m}]^{\mathsf{T}}$ with a 12° tilt angle, where the UE is placed at several different positions. Among $\boldsymbol{s}_{\text{UE},l}$ $x_{\text{UE},l}$ varies within $[0\text{ m}, 80\text{ m}]$, $y_{\text{UE},l}$ varies within $[-40\text{ m}, 40\text{ m}]$, $z_{\text{UE},l}$ varies within $[-2\text{ m}, 2\text{ m}]$, $\alpha_{\text{UE},l}$ varies within $[-2°, 2°]$, $\beta_{\text{UE},l}$ varies within $[-5°, 5°]$, and $\gamma_{\text{UE},l}$ varies within $[-45°, 45°]$, as the heights, rolls and pitches do not seriously change on the road. We generate a group of measurement from each BS location. The prior of the UE $p(\boldsymbol{p}_{\text{BS}})$ is a uniform distribution over the space. The BS orientation is given, and we only estimate $p(\boldsymbol{p}_{\text{BS}})$. The standard deviation of each dimension of the GPS measurement is set as the corresponding accuracy shown in Table. I. As there is no ability to estimate AOA elevation, we only consider AOA azimuth and AOD azimuth and elevation angles, with the resolutions $4.5°$, $4°$, and $7°$ (approximated from the beam-width). Overall, 100 Monte Carlo (MC) simulations are performed, and the results are obtained by averaging over the different MC simulations. We evaluated the BS localization performance by the mean absolute value (MAE) over all MC simulations. This analysis will then tell us if the test results are in a meaningful range.

C. Results and Discussion

1) Channel estimation: We firstly visualize the channel estimation algorithm by showing the channel estimation results of typical received signals at static test location P1, as shown in Fig. 7. Fig. 7(a) shows the energy heatmap of the BS-UE beam pairs from channel estimation, where two strong beam pairs (27, 11) and (31, 3) can be clearly observed. By sorting these beam pairs and taking the top-100 beams with the highest energy, the energy (in dB) of each beam is shown in Fig. 7(b). The delay of each beam pair can also be obtained as shown in Fig. 7(c), where the delay (relative delay due to the clock

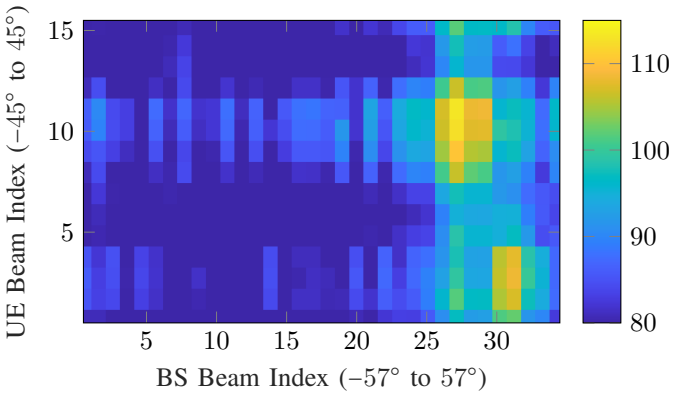

(a) The energy heatmap of BS-UE beam pairs.

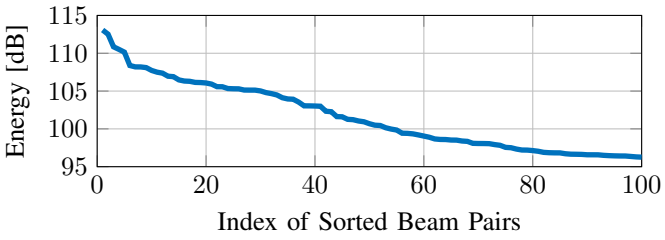

(b) The energy of each beam.

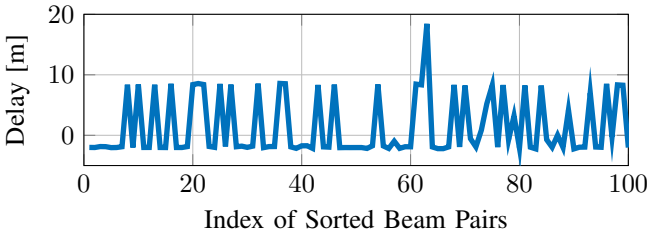

(c) The delay of each beam.

Fig. 7. Channel estimation results for typical receive signals. Two strong paths can be seen from the beamspace heatmap in (a), which is verified in the delay estimations in (c).

offset) of the LOS path and NLOS path are around -2 m and 8 m, matching the two strong beams in the beam pair heatmap in Fig. 7(a) and the 10 m TDOA shown in Fig. 6. We then apply the channel estimator to the real received signals and picked at the paths of the shortest delay of each group of data, which are the LOS paths and will be input into the BS localization algorithm.

2) Test localization results: We implemented the BS localization algorithm on the channel estimates of the real measurements. We recall that since the UE and BS are not synchronized, the LOS path only provides information via the AOA and AOD. We find that the overall error is 24.82 m, based on the measurements from P1 and P2 in Fig. 6. This is because although there are 20 measurements in total, they are from only 2 different locations, hence measurements from the same locations are highly correlated. Only knowing the BS direction with respect to the two different UE locations, the BS location is found by the intersection point of the two

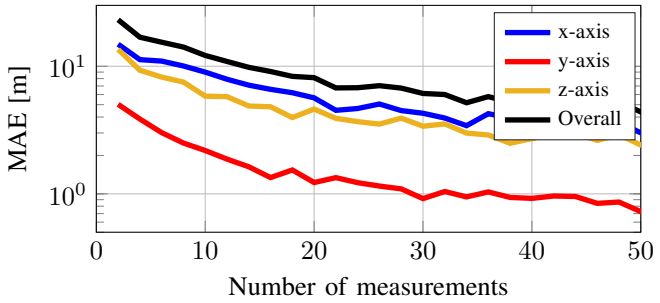

Fig. 8. The overall performance and the performance on different dimensions of the BS localization using different numbers of measurements under similar settings as the experiment.

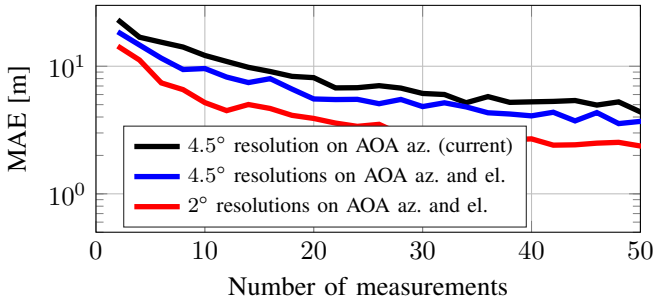

Fig. 9. The comparison among the overall performances of three different cases.

corresponding lines, which is sensitive to the angle errors, especially at a long distance.

3) Simulated localization results: We analyze (in simulation) the overall performance and the performance on different dimensions of the BS localization using different numbers of measurements from various UE locations under similar settings as the test, as shown in Fig. 8. We observe that under the current settings, the error is around 23 m when having only 2 measurements from different UE locations, which corresponds to the results of real measurements. We also observed that under the current settings at least 14 measurements from different UE locations are required to have below 10 m accuracy, and the accuracy can reach 3 m levels if there are enough measurements from different UE locations. It is impossible to do BS localization using only one snapshot. This is because we only know which direction the BS is on with respect to the UE, but we do not know how far away the BS should be alongside this direction.

We also analyze the performances of the BS localization of two other cases and compare with the current settings, where we provide the AOA elevation estimates with the resolution of 4.5°, and a high resolution case with the resolution 2° on both AOA azimuth and elevation angles, as shown in Fig. 9. We observe that having a higher resolution on AOA elevation and azimuth can improve the BS localization performance, as the red curve is lower than the blue curve, followed by the black curve. If a 4.5° resolution on AOA elevation is provided, the error is below 10 m/5 m/2.5 m when having 8/30/100 measurements from different UE locations. For the high resolution case, the error can reach below 3 m when having more than 30 measurements from different UE locations, and below 1.5 m when having 100 measurements from different UE locations.

Therefore, in future experiments, we aim to place the UE at more than 30 different locations to collect measurements, change the receiver antenna element placement and beam patterns to have a higher resolution on AOA elevation, apply other channel estimation algorithms to provide better channel estimations, and exploit NLOSs and TDOAs.

VI. Conclusions

In this paper, we present the experimental setup, and report some initial results, for our work towards validation of single-BS vehicular positioning with downlink 5G mmWave signals. An approach for measurement validation is presented, where the position of the BS is estimated based on a set of LOS measurements made at known UE locations. The presented method can also be used when the exact position of the BS is unknown or provided with significant uncertainties. Additionally, based on the presented signal model, MC simulations provide insights on what is required from the measurement set. These insights will provide input to upcoming measurements, impacting receiver antenna configuration as well as the number of measurement positions.

Acknowledgment

This work was partially supported by the Vinnova 5GPOS project under grant 2019-03085, by the Swedish Research Council under grant 2018-03705, and the Wallenberg AI, Autonomous Systems and Software Program (WASP) funded by Knut and Alice Wallenberg Foundation.

References

[1] V. Ilci and C. Toth, "High definition 3D map creation using GNSS/IMU/LiDAR sensor integration to support autonomous vehicle navigation," *Sensors*, vol. 20, no. 3, p. 899, 2020.

[2] N. Joubert, T. G. Reid, and F. Noble, "Developments in modern GNSS and its impact on autonomous vehicle architectures," in *IEEE Intelligent Vehicles Symposium (IV)*, 2020, pp. 2029–2036.

[3] E. Javanmardi, M. Javanmardi, Y. Gu, and S. Kamijo, "Factors to evaluate capability of map for vehicle localization," *IEEE Access*, vol. 6, pp. 49 850–49 867, 2018.

[4] J. Einsiedler, I. Radusch, and K. Wolter, "Vehicle indoor positioning: A survey," in *14th Workshop on Positioning, Navigation and Communications (WPNC)*, 2017, pp. 1–6.

[5] J. A. del Peral-Rosado, R. Raulefs, J. A. López-Salcedo, and G. Seco-Granados, "Survey of cellular mobile radio localization methods: From 1G to 5G," *IEEE Communications Surveys & Tutorials*, vol. 20, no. 2, pp. 1124–1148, 2017.

[6] H. Wymeersch, G. Seco-Granados, G. Destino, D. Dardari, and F. Tufvesson, "5G mmWave positioning for vehicular networks," *IEEE Wireless Communications*, vol. 24, no. 6, pp. 80–86, 2017.

[7] 3GPP, "Study on NR positioning support," TR 38.855, Technical Report 16.0.0, 2019.

[8] S. Dwivedi, R. Shreevastav, F. Munier, J. Nygren, I. Siomina, Y. Lyazidi, D. Shrestha, G. Lindmark, P. Ernström, E. Stare, *et al.*, "Positioning in 5G networks," *IEEE Communications Magazine*, vol. 59, no. 11, pp. 38–44, 2021.

[9] M. Posluk, J. Ahlander, D. Shrestha, S. M. Razavi, G. Lindmark, and F. Gunnarsson, "5G deployment strategies for high positioning accuracy in indoor environments," *arXiv preprint arXiv:2105.09584*, 2021.

[10] G. Yammine, M. Alawieh, G. Ilin, M. Momani, M. Elkhouly, P. Karbownik, N. Franke, and E. Eberlein, "Experimental investigation of 5G positioning performance using a mmWave measurement setup," in *International Conference on Indoor Positioning and Indoor Navigation (IPIN)*, 2021, pp. 1–8.

[11] F. Mata, F. Grec, M. Azaola, F. Blázquez, A. Fernández, E. Dominguez, G. Cueto-Felgueroso, G. Seco-Granados, J. del Peral-Rosado, E. Staudinger, *et al.*, "Preliminary field trials and simulations results on performance of hybrid positioning based on GNSS and 5G signals," in *Proceedings of the 33rd International Technical Meeting of the Satellite Division of The Institute of Navigation (ION GNSS+)*, 2020, pp. 387–401.

[12] R. Keating, M. Säily, J. Hulkkonen, and J. Karjalainen, "Overview of positioning in 5G new radio," in *16th International Symposium on Wireless Communication Systems (ISWCS)*, 2019, pp. 320–324.

[13] K. Witrisal, P. Meissner, E. Leitinger, Y. Shen, C. Gustafson, F. Tufvesson, K. Haneda, D. Dardari, A. F. Molisch, A. Conti, *et al.*, "High-accuracy localization for assisted living: 5G systems will turn multipath channels from foe to friend," *IEEE Signal Processing Magazine*, vol. 33, no. 2, pp. 59–70, 2016.

[14] A. Shahmansoori, G. E. Garcia, G. Destino, G. Seco-Granados, and H. Wymeersch, "Position and orientation estimation through millimeter-wave MIMO in 5G systems," *IEEE Transactions on Wireless Communications*, vol. 17, no. 3, pp. 1822–1835, 2018.

[15] R. Mendrzik, H. Wymeersch, G. Bauch, and Z. Abu-Shaban, "Harnessing NLOS components for position and orientation estimation in 5G millimeter wave MIMO," *IEEE Transactions on Wireless Communications*, vol. 18, no. 1, pp. 93–107, 2019.

[16] J.-L. Blanco, "A tutorial on SE (3) transformation parameterizations and on-manifold optimization," *University of Malaga, Tech. Rep*, vol. 3, p. 6, 2010.

[17] R. W. Heath, N. Gonzalez-Prelcic, S. Rangan, W. Roh, and A. M. Sayeed, "An overview of signal processing techniques for millimeter wave MIMO systems," *IEEE Journal of Selected Topics in Signal Processing*, vol. 10, no. 3, pp. 436–453, 2016.

[18] 3GPP, "Physical channels and modulation," TS 38.211, Technical Specification 16.2.0, 2020.

[19] F. Wen, H. C. So, and H. Wymeersch, "Tensor decomposition-based beamspace ESPRIT algorithm for multidimensional harmonic retrieval," in *IEEE ICASSP*, Barcelona, Spain, 2020.

[20] J. Zhang and M. Haardt, "Channel estimation and training design for hybrid multi-carrier mmwave massive MIMO systems: The beamspace esprit approach," in *IEEE EUSIPCO*, Kos, 2017.

[21] F. Jiang, F. Wen, Y. Ge, M. Zhu, H. Wymeersch, and F. Tufvesson, "Beamspace multidimensional ESPRIT approaches for simultaneous localization and communications," *arXiv:2111.07450v1*, 2021.

[22] O. T. S. Ltd. (2022) RT3000 v2. [Online]. Available: https://www.oxts.com/software/navsuite/documentation/datasheets/RT3000v2_ds.pdf

[23] Lantmäteriet. (2022) Nätverks-rtk. [Online]. Available: https://www.lantmateriet.se/sv/Kartor-och-geografisk-information/gps-geodesi-och-swepos/swepos/swepos-tjanster/natverks-rtk/